iScience

CellPress
OPEN ACCESS

Article

Interfacial transport modulation by intrinsic potential difference of janus TMDs based on $CsPbI_3$/J-TMDs heterojunctions

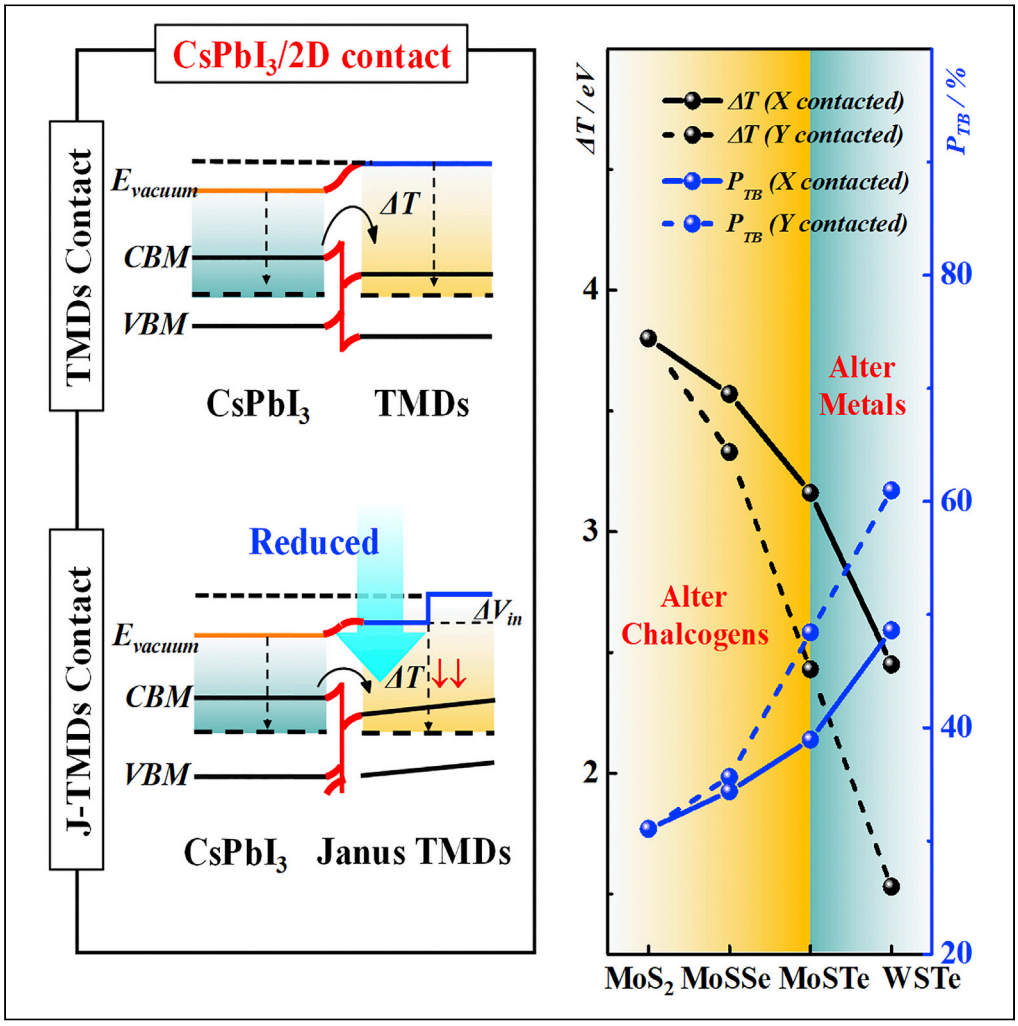

Haidong Yuan, Jie Su, Siyu Zhang, ..., Jie Zhang, Jingjing Chang, Yue Hao

jjingchang@xidian.edu.cn (J.C.)
sujie@xidian.edu.cn (J.S.)

Highlights

An intrinsic potential difference (ΔV_{in}) exists in asymmetrical Janus TMD (J-TMD)

A reversible type-II band alignment realized by modulating the contact configuration

The transport performance of $CsPbI_3$/J-TMD heterojunction directly determined by ΔV_{in}

The optical absorption is enlarged by modulating the direction and intensity of ΔV_{in}

Yuan et al., iScience 25, 103872
March 18, 2022
https://doi.org/10.1016/j.isci.2022.103872

iScience

CellPress
OPEN ACCESS

Article

Interfacial transport modulation by intrinsic potential difference of janus TMDs based on $CsPbI_3$/J-TMDs heterojunctions

Haidong Yuan,[1] Jie Su,[2,*] Siyu Zhang,[1] Jiayu Di,[1] Zhenhua Lin,[1] Jincheng Zhang,[1] Jie Zhang,[1,2,3] Jingjing Chang,[1,4,*] and Yue Hao[1]

SUMMARY

Although perovskite/two-dimensional (2D) materials heterojunctions have been employed to improve the optoelectronic performance of perovskite photodetectors and solar cells, effects of the intrinsic potential difference (ΔV_{in}) of asymmetrical 2D materials, like Janus TMDs (J-TMDs), were not revealed yet. Herein, by investigating the optoelectronic properties of $CsPbI_3$/J-TMDs heterojunctions, we find a reversible type-II band alignment related to the intensity and direction of ΔV_{in}, suggesting that carrier transport paths can be reversed by modulating the contact configuration of J-TMDs in the heterojunctions. Meanwhile, the band offset, carrier transfer efficiency and optical properties of those heterojunctions are directly determined by the intensity and direction of ΔV_{in}. Overall, $CsPbI_3$/MoSSe heterojunction is suggested in this work with a tunneling probability of 79.65%. Our work unveils the role of ΔV_{in} in asymmetrical 2D materials on the optoelectronic performances of lead halide perovskite devices, and provides a guideline to design high performance perovskite optoelectronic devices.

INTRODUCTION

In recent years, lead halide perovskites have attracted great attention in the application of high-performance photovoltaic and optoelectronic because of their large optical absorption coefficient, low cost, simple preparation, etc. (Gu et al., 2020; Guzelturk et al., 2021; Tao et al., 2021, 2020; Wang et al., 2021a; Wang et al., 2020) Photodetectors based on lead halide perovskites have been widely applied in diverse fields including optical communication, remote sensing, military surveillance, imaging technology, and industry automation control. However, it should be noted that the organic-inorganic lead halide perovskite possesses the poor stability which hinders the development of perovskite devices (Li et al., 2019; Zhou and Zhao, 2019). Alternatively, all-inorganic cesium lead halide perovskite ($CsPbX_3$) not only shows a more effective stability (Jiang et al., 2018; Seth et al., 2019), but also demonstrates excellent optoelectronic properties, such as direct optical band gaps, large optical absorption, and high luminescence efficiency (Nedelcu et al., 2015; Protesescu et al., 2015). These optoelectronic properties make $CsPbX_3$, especially $CsPbI_3$, promising for solar cells, light-emitting diodes, lasers, and photodetectors (Liu et al., 2021; Zhang et al., 2015).

To further improve the optoelectronic performance of perovskite devices, heterojunction engineering, especially perovskite/2D material heterojunction has been becoming an effective approach (Zhang et al., 2021). For instance, $CH_3NH_3PbI_3$/graphene heterojunction not only broadened the spectral photoresponsivity of perovskite photodetector, but also increased the effective quantum efficiency to 5×10^4% under an illumination power of 1 μW (Lee et al., 2015). Moreover, $CsPbBr_3/MoS_2$ heterojunction could increase the photoresponsivity and photodetectivity to 4.4 A/W and 2.5×10^{10} Jones, respectively, because of the high efficient photoexcited carrier separation at the interface between MoS_2 and $CsPbBr_3$ (Song et al., 2018). $CsPbI_3$/phosphorus heterojunctions enhanced the light absorptions especially in the infrared region (Liu et al., 2018).

Compared to the symmetrical 2D materials, 2D asymmetrical polar materials Janus TMDs (J-TMDs, namely, MXY, M = Mo, W; X = S; Y=S, SE, Te in this work), which can be prepared by selenization or tellurization of symmetrical MoS_2 in experiment (Lu et al., 2017; Yun et al., 2017), not only possess excellent optical

[1]State Key Discipline Laboratory of Wide Band Gap Semiconductor Technology, Shaanxi Joint Key Laboratory of Graphene, School of Microelectronics, Xidian University, 2 South Taibai Road, Xi'an, 710071 China

[2]Jiangsu Key Lab of Advanced Food Manufacturing Equipment and Technology, Jiangnan University, Wuxi, 214122 China

[3]Center of Micro-Nano Engineering, School of Mechanical Engineering, Jiangnan University, Wuxi, 214122 China

[4]Lead contact

*Correspondence: jjingchang@xidian.edu.cn (J.C.), sujie@xidian.edu.cn (J.S.)

https://doi.org/10.1016/j.isci.2022.103872

absorption, tunable band gap, high carrier mobility, but also have the intrinsic potential difference (ΔV_{in}) of J-TMDs by destroying the out-of-plane mirror symmetry which can be regarded as another degree of freedom for modulating their properties (Yin et al., 2021). Moreover, such intrinsic ΔV_{in} has been found to promote the electron-hole separation, band levels variation, and mobility modulation, resulting in effective inhibition of carrier recombination and enhancement of responsivity (Dong et al., 2017; Er et al., 2018; Li et al., 2018; Lian et al., 2019; Thanh et al., 2020; Zhang et al., 2020; Zhou et al., 2019). Inspired by these, it is thought that the optoelectronic performances of perovskite devices based on perovskite/TMDs heterojunctions may be further improved by the intrinsic ΔV_{in} when the TMDs are replaced by the J-TMDs.

Herein, $CsPbI_3$/J-TMDs (MXY, M = Mo, W; X = S; Y=S, SE, Te) heterojunctions are studied to unveil the roles of ΔV_{in} in J-TMDs on the optoelectronic properties of $CsPbI_3$ based device. The results demonstrate that all $CsPbI_3$/J-TMDs heterojunctions in this work have a type-II band alignment, indicating that charge transfer rather than energy transfer dominates in $CsPbI_3$/J-TMDs heterojunctions. Moreover, a reversed type-II band alignment happened when ΔV_{in} deviates from the interface and increases further, suggesting that carrier transport paths can be reversed by modulating the contact configuration of J-TMDs in the heterojunctions. A better optoelectronic performance was found in the heterojunction based on PbI configuration rather than CsI configuration, resulting from the former higher work function and more complete structural framework. Meanwhile, the band offset, carrier transfer efficiency, and optical properties are directly dependent on both the intensity and direction of ΔV_{in}. In addition, the heterojunction with a larger ΔV_{in} pointing away from the interface possesses a smaller band offset with higher carrier transfer efficiency and optical absorption. $CsPbI_3$/MoSSe heterojunction is recommended with a tunneling probability (P_{TB}) of 79.65%. Our work unveils the role of intrinsic ΔV_{in} in asymmetrical polar 2D materials on the optoelectronic performances of perovskite devices, and provides a guideline to design high performance perovskite optoelectronic devices.

RESULTS AND DISCUSSION

Isolated $CsPbI_3$ surfaces and monolayer J-TMDs

Before investigating the electronic structures of $CsPbI_3$/J-TMDs heterojunctions, the electronic structures of their isolated surfaces are calculated by PBE and HSE06 functionals. In addition, the calculated lattice parameters are listed in Table S1 and consistent with previous experimental and theoretical results. The calculated projected band structures and corresponding parameters of those isolated surfaces are illustrated in Figure S1 (PBE), Figure 1 (HSE06), and Table 1. It can be found that electronic structures of those isolated surfaces calculated by PBE and HSE06 functionals are similar except for bandgaps, where the bandgaps calculated by HSE06 functional are consistent with experimental values. Therefore, HSE06 functional is mainly applied to investigate the electronic structure of $CsPbI_3$/J-TMDs heterojunctions in this work.

Here, two types of $CsPbI_3$ surface namely CsI and PbI surface are considered, as shown in Figure 1A. The CsI and PbI surfaces have a direct bandgap with 1.75 and 1.83 eV, respectively, which are consistent with the previous studies (Liu et al., 2018). The conduction band minimum (CBM) and valence band maximum (VBM) of both the CsI and PbI surfaces are dominated by Pb *p*-orbitals and I *p*-orbitals, respectively, as is illustrated in Figures S2A and S2B. As for the effective masses m_e^* and m_h^*, they are 0.19 and 0.29 m_0 for CsI surface, whereas 0.18 and 0.26 m_0 for PbI surface, respectively; such effective masses are consistent with previous research (He et al., 2019). Correspondingly, the exciton binding energy E_x calculated is 106.21 meV for CsI surface which is larger than that of 77.98 meV for PbI surface, indicating a poor carries recombination for CsI surface compared with the PbI surface. In addition, as listed in Table S2, the energies of E_{CsI} and E_{PbI} surfaces are −57.17 and −58.96 eV, respectively, suggesting that the PbI surface is much more stable than the CsI surface.

For J-TMDs monolayer, their electronic structures are displayed in Figures 1D–1G and S2C–S2F. MoS_2 monolayer has a direct bandgap with 2.01 eV, and its CBM and VBM are mainly consisted of Mo-*d* orbitals and a little contribution of S-*p* orbitals, which are consistent with previous reports (Kadantsev and Hawrylak, 2012; Santos and Kaxiras, 2013). It is thought that both the electron and hole are transported at the Mo-S bonds. The calculated effective masses m_e^* and m_h^* of MoS_2 are 0.41 and 0.48 m_0, leading to the exciton binding energy of 262.21 meV, which are consistent with previous studies (Park et al., 2018; Pedersen et al., 2016). For J-TMDs, evident intrinsic potential difference (ΔV_{in}) points from the heavy atoms Y side to light atoms X side are observed, as marked in Figures 1H and S3. The ΔV_{in}s are 0.61, 1.34, and 1.38 eV for Janus

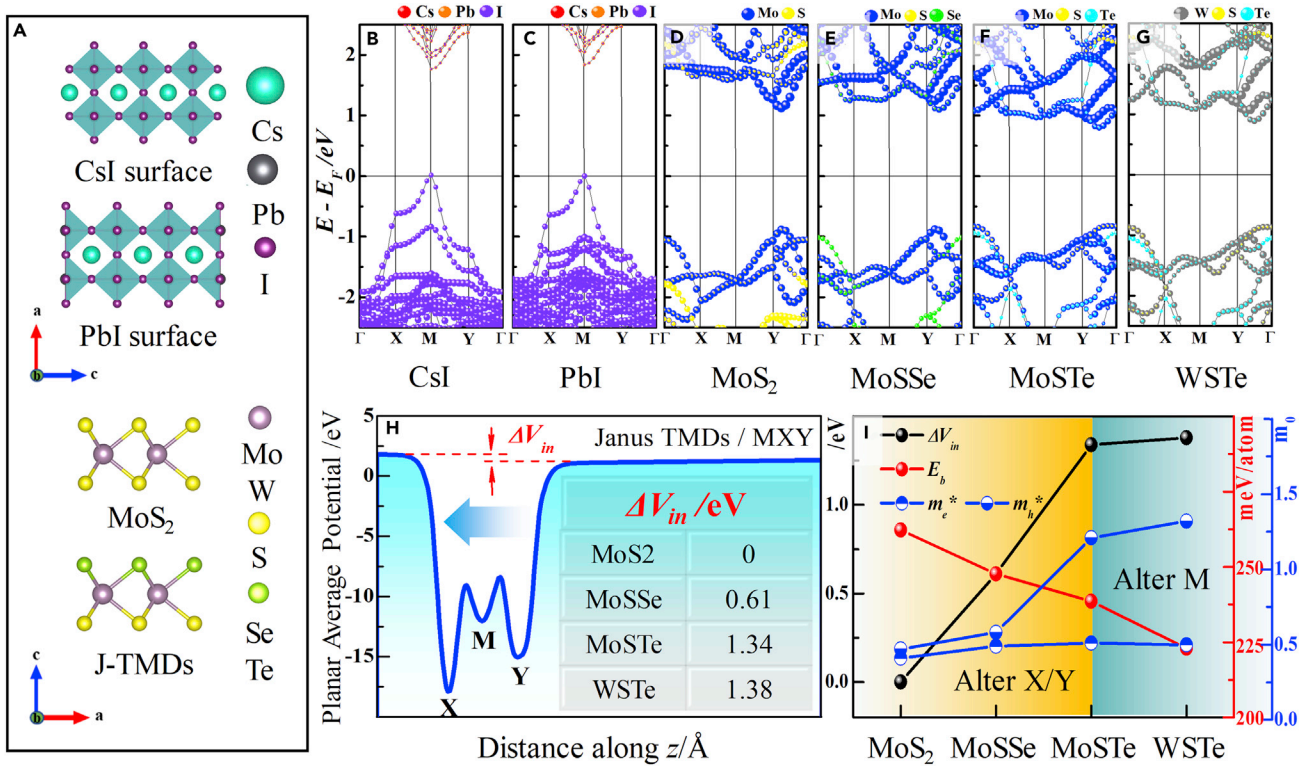

Figure 1. The structure models and electronic structures od isolated $CsPbI_3$ and J-TMDs

(A) The structure models for $CsPbI_3$ surfaces and J-TMDs monolayers.

(B) Electronic band structures of CsI surface.

(C) Electronic band structures of PbI surface.

(D) Electronic band structures of MoS_2 monolayer.

(E) Electronic band structures of MoSSe monolayer.

(F) Electronic band structures of MoSTe monolayer.

(G) Electronic band structures of WSTe monolayer.

(H) Planar-averaged electrostatics potentials of Janus TMDs along the direction normal to the interface region.

(I) Exciton binding energies and effective masses of Janus TMDs as functions of the ΔV_{in}

MoSSe, MoSTe, and WSTe, respectively, indicating that ΔV_{in} can be enhanced significantly by altering the chalcogens (X) or enhanced slightly by altering the metals (M) of J-TMDs. As a result, the CBMs of J-TMDs are dominated by the hybrid orbitals between M *d*-orbitals and *p*-orbitals of heavy Y, whereas the VBMs are dominated by the hybrid orbitals between M *d*-orbitals and *p*-orbitals of light X, as demonstrated in Figures 1D–1G and S2C–S2F. It is thought that electrons and holes of J-TMDs are transported at the M−Y and M-X bonds, respectively, indicating an excellent ability of electron-hole separation for J-TMDs (Tao et al., 2019; Thanh et al., 2020). It is noted that MoSSe has a direct bandgap with 1.97 eV, whereas MoSTe and WSTe have an indirect bandgap with 1.62 and 1.75 eV, respectively. The bandgap of J-TMD reduces with the enlarging ΔV_{in} by altering the X of J-TMDs, whereas an opposite character occurs while altering the M of J-TMDs. On the contrary, the effective masses significantly increase with the enhancing ΔV_{in} by altering the X of J-TMDs, whereas they are slightly enlarged as the variation of ΔV_{in} induced by altering X, as listed in Table 1 and Figure 1I. It is noted that variation of m_e* and m_h* of J-TMDs are strongly and slightly tuned by the ΔV_{in} of J-TMDs. As a result, the exciton binding energies of J-TMDs are lower than that of MoS_2 monolayer, indicating the weaker carrier recombination for J-TMDs. Moreover, the exciton binding energies of J-TMDs decrease monotonously with the increasing ΔV_{in} of J-TMDs. Moreover, Table S2 lists out the energies of those $E_{J\text{-}TMDs}$; the stability of J-TMDs changes to worse as the intrinsic ΔV_{in} increases while being altered by chalcogens, and changes to better when ΔV_{in} is being altered by metals. Hence, J-MoSSe seems to be a better choice because of its perfect properties and easy selenization of MoS_2 in experiment. Such dependence of electronic and transport properties of J-TMDs on the strength

Table 1. Bandgaps, effective masses and exciton energies of isolated surface of $CsPbI_3$ and J-TMDs monolayers

		$CsPbI_3$					
Isolated surface		CsI	PbI	MoS_2	MoSSe	MoSTe	WSTe
Band gap/eV	HSE06	1.75	1.83	2.01	1.97	1.62	1.75
	PBE	1.34	1.43	1.53	1.32	1.04	1.21
	Experimental	1.73		1.98	–	–	–
m_e^*/m_0		0.19	0.18	0.41	0.49	0.51	0.57
m_h^*/m_0		0.29	0.26	0.48	0.58	1.21	1.32
E_x/meV		106.21	77.98	262.21	247.69	238.61	222.92

of intrinsic ΔV_{in} expands the tunability of optoelectronic properties and application of 2D material in $CsPbI_3$/2D heterojunctions.

Binding energies

Figure S4 shows the structure models of $CsPbI_3$/J-TMDs heterojunctions, and Figure S5 illustrates the binding energies (E_b) as functions of the interlayer separation. For $CsPbI_3/MoS_2$ heterojunction, when the interlayer separations of with CsI/MoS_2 and PbI/MoS_2 heterojunctions are 3.2 and 3.4 Å, respectively, binding energies of corresponding CsI/MoS_2 and PbI/MoS_2 heterojunctions reach to the lowest negative values of about −0.039 and −0.109 eV/atom, as listed in Table S3. It indicates that the $CsPbI_3/MoS_2$ heterojunctions, in particular the PbI/MoS_2 heterojunction, with such interlayer separations are stable and possible to be fabricated in experiment, which is consistent with previous reports (He et al., 2019).Similar to the $CsPbI_3$/MoS_2 heterojunction, the larger interlayer distances and lower binding energies are observed for PbI/MoS_2 heterojunctions than CsI/MoS_2 heterojunctions, suggesting the more stable for PbI/MoS_2 heterojunctions than CsI/MoS_2 heterojunctions. Moreover, it is interesting that the interlayer separations of $CsPbI_3$/J-TMDs heterojunctions are dependent on the interfacial contact character, where the interlayer separation of interface contacted by light atoms X is shorter than that contacted by heavy atoms Y. Such opposite phenomenon is suitable to the binding energies for $CsPbI_3$/J-TMDs heterojunctions. For examples, the equilibrium interlayer separations and binding energies of CsI/S-MoSSe and CsI/Se-MoSSe heterojunctions are 3.2 Å and 0.060 eV/atom, and 3.4 Å and 0.038 eV/atom, respectively. Moreover, all the interlayer separations are higher than the sum of radii of Pb (or Cs) and X (or Y) atoms, suggesting the van der Waals heterojunction for $CsPbI_3$/J-TMDs heterojunctions. Except for the interfacial contact character, the intrinsic potential differences of J-TMDs also affect the binding energies of $CsPbI_3$/J-TMDs heterojunctions, where the E_b increases with the increment of ΔV_{in}, as listed in Table S3. It suggests the poor stability for the $CsPbI_3$/J-TMDs heterojunctions with large intrinsic potential difference.

Electronic structures

Figures 2A and S6A illustrate the projected band structures of CsI/J-TMDs and CsI/J-TMDs heterojunctions, respectively. It can be found that the electronic band structures of CsI/J-TMDs heterojunctions seem to be a simple sum of electronic band structures isolated CsI surface and J-TMDs monolayer, irrespective of heterojunction configurations. For example, the bandgaps of $CsPbI_3$ and MoS_2 parts for CsI/MoS_2 heterojunctions are 1.79 and 1.97 eV (see Table 2), respectively, which are close to those of the isolated CsI surface (1.75 eV) and MoS_2 monolayer (2.01 eV). Moreover, as shown in Figures 3 and S7, the CBM and VBM of isolated CsI part of CsI/MoS_2 heterojunctions are dominated by Pb *p*-orbitals and I *p*-orbitals, respectively; the CBM and VBM of isolated MoS_2 part of CsI/MoS_2 heterojunctions both are dominated by Mo *d*-orbitals and S p-orbitals. The effective masses and exciton binding energy of CsI part and MoS_2 part of CsI/MoS_2 heterojunctions are 0.26 m_0 of m_h^* and 101.61 meV, and 0.43 m_0 of m_e^* and 270.12 meV, respectively. These are close to those of isolated CsI surface and MoS_2 monolayer, as listed in Tables 1 and 2. These phenomena are the typical characters for vdW heterojunction, suggesting the CsI/MoS_2 vdW heterojunction. Similar characters are also observed for other CsI/J-TMDs vdW heterojunctions, no matter how the intrinsic ΔV_{in}s and contact characters of J-TMDs change, as demonstrated in Figure 2 and Table 2.

In addition, the VBM and CBM of CsI/J-TMDs heterojunctions are located at the perovskite (or J-TMD) parts and J-TMD (or perovskite) parts of heterojunctions, indicating the type-II band characters for all

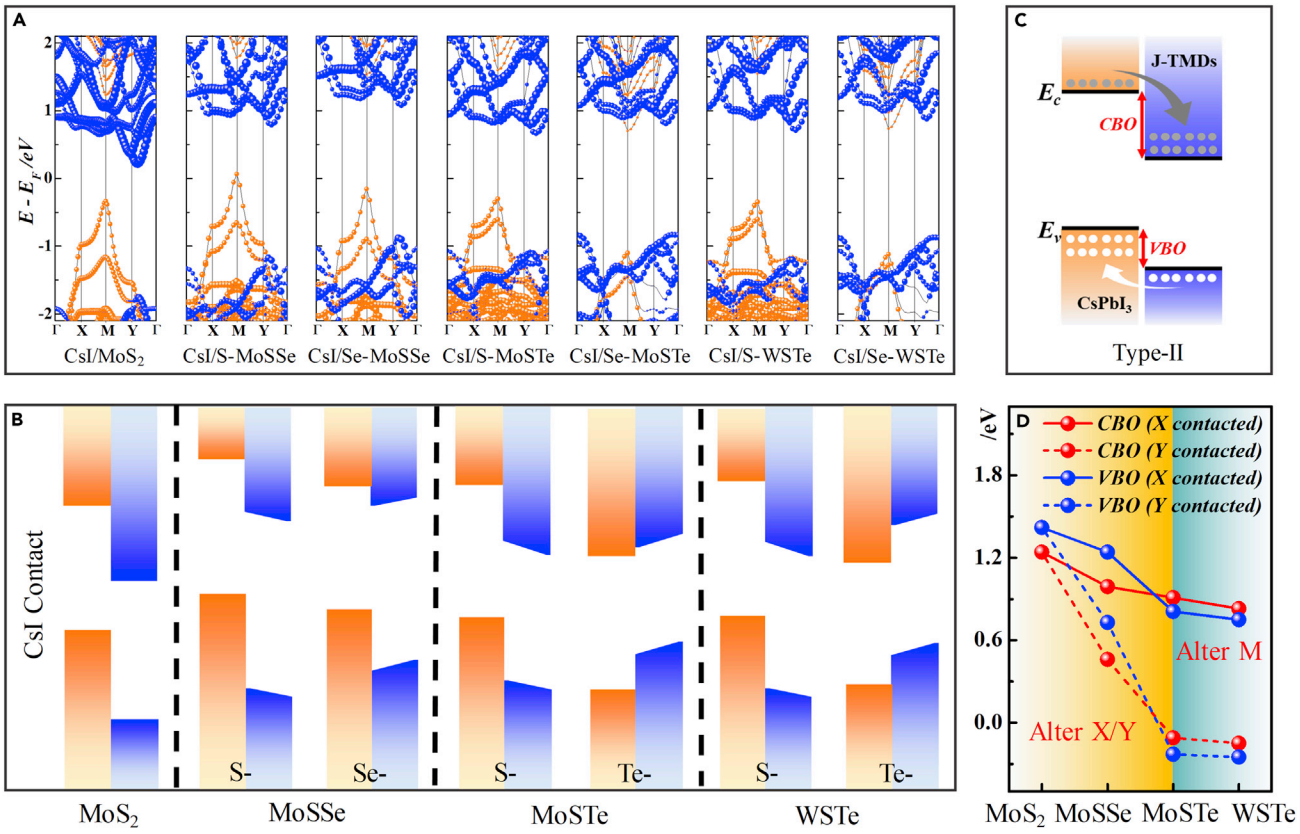

Figure 2. The electronic structures of CsI/J-TMDs heterojunctions

(A) Projected band structures of CsI/J-TMDs heterojunctions.

(B) Schematic diagram of band alignment for CsI/J-TMDs heterojunctions.

(C) Schematic diagram of type-II heterojunctions.

(D) The band offsets of CsI/J-TMDs heterojunctions as a function of intrinsic ΔV_{in}

CsI/J-TMDs heterojunctions, as shown in Figures 2C and S6C. For example, the VBM and CBM of CsI/MoS_2 heterojunctions are located at the CsI surface and MoS_2 part, respectively, which are in good agreement with previous reports (He et al., 2019). It is thought that a strong ability of this heterojunction to move free electrons from perovskite to MoS_2 part, and promote hole extraction from MoS_2 part to perovskite surface. The conduction band offset (CBO) and valence band offset (VBO) of CsI/MoS_2 heterojunctions are 1.24 and 1.42 eV, respectively. When the MoS_2 layer with symmetrical structure is replaced by the J-TMD with asymmetrical structure, both the CBO and VBO of CsI/J-TMDs heterojunctions are reduced. Moreover, the band offsets, in particular the VBO, continue to decrease as the intrinsic potential difference (ΔV_{in}) of J-TMD enlarges, as illustrated in Figure 2D. It is interesting that the decrement of CsI/J-TMDs heterojunction with heavy atom contact is stronger than that of CsI/J-TMDs heterojunction with light atom contact. As a result, the band offsets of type-II CsI/J-TMDs heterojunction with heavy atom contact are easy to turn into negative values, but the band offsets of type-II CsI/J-TMDs heterojunction with light atom contact keep positive values. It means that carrier transport paths of CsI/J-TMDs heterojunctions can be reversed by modulating the contact configuration of J-TMDs in the heterojunctions, although the CsI/J-TMDs heterojunctions remain the type-II band characters, as demonstrated in Figure S6C. Taking the CsI/MoSTe heterojunction as an example, the CBO (VBO) of CsI/Te-MoSTe heterojunction of about −0.11 eV (−0.23 eV) is smaller than that of CsI/S-MoSTe heterojunction of about 0.91 eV (0.81 eV), which are lower than that of CsI/MoS_2 heterojunction of about 1.24 eV (1.42 eV). Moreover, photo-generated electron and hole of CsI/Te-MoSTe heterojunction are transport at $CsPbI_3$ surface and MoSTe parts of heterojunctions, which are inverse to the CsI/S-MoSTe heterojunction whose photo-generated electron and hole are transport at the MoSTe and $CsPbI_3$ parts, respectively. It is noted that the band offset of type-II heterojunction indicates the driving force and efficiency of carrier transfer at the type-II heterojunction.

Table 2. The detailed bandgaps, CBM, VBM and effective masses (m_0) of $CsPbI_3$/J-TMDs heterojunctions

Contacted surface		MoS_2	MoSSe		MoSTe		WSTe	
			S-	Se-	S-	Te-	S-	Te-
CsI-	$E_{g\ (CsI)}$	1.79	1.72	1.69	1.90	1.80	1.89	1.85
	$E_{g\ (MXY)}$	1.97	1.96	1.96	1.73	1.64	1.92	1.75
	CBM	Mo-*d*	Mo-*d*	Mo-*d*	Mo-*d*	Cs-*p*	Mo-*d*	Cs-*p*
	VBM	I-*p*	I-*p*	I-*p*	I-*p*	Mo-*d*	I-*p*	Mo-*d*
	m_e*	0.43	0.59	0.61	0.55	0.20	0.55	0.15
	m_h*	0.26	0.23	0.22	0.23	1.28	0.34	1.23
PbI-	$E_{g\ (CsI)}$	1.76	1.80	1.88	1.96	1.94	2.04	2.02
	$E_{g\ (MXY)}$	2.05	1.96	1.85	1.49	1.52	1.57	1.58
	CBM	Mo-*d*	Mo-*d*	Mo-*d*	Mo-*d*	Cs-*p*	Mo-*d*	Cs-*p*
	VBM	I-*p*	I-*p*	I-*p*	I-*p*	Mo-*d*	I-*p*	Mo-*d*
	m_e*	0.41	0.66	0.61	0.54	0.21	0.50	0.18
	m_h*	0.29	0.24	0.19	0.20	1.36	0.25	1.47

It suggests that the lower driving force and efficiency of electron (or hole) transfer from CsI surface (or J-TMDs layer) to J-TMDs layer (or CsI surface) for CsI/J-TMDs heterojunctions, in particular the heterojunctions with heavy atom contact, compared to those of CsI/MoS_2 heterojunctions. Note that the direction of intrinsic ΔV_{in}s of J-TMD points from the heavy atomic layer to the light atomic layer of J-TMD. Thus, it is thought that the decrements of band offsets for CsI/J-TMDs heterojunctions are dependent of the direction and amount of intrinsic ΔV_{in}s of J-TMDs layers in the heterojunctions, where the CsI/J-TMDs heterojunctions show smaller band offsets when the directions of intrinsic ΔV_{in}s of J-TMDs layers point away from the contact region than those point to the contact region. In addition, because the intrinsic ΔV_{in}s of J-TMDs are significantly and gradually tuned by altering the chalcogens and metals of J-TMDs, respectively (see Figure 1), the band offsets of CsI/J-TMDs heterojunctions can be severely reduced by altering the chalcogens of J-TMDs, whereas they are slightly reduced by altering the metals of J-TMDs.

Compared to the CsI/J-TMDs heterojunctions, similar characters are observed for the PbI/J-TMDs vdW heterojunctions. However, the band offsets of PbI/J-TMDs vdW heterojunctions are larger than those of CsI/J-TMDs heterojunctions. Moreover, the variations of band offsets for PbI/J-TMDs vdW heterojunctions are more significantly tuned by the direction and strength of intrinsic potential difference than those of CsI/J-TMDs heterojunctions, as comparatively illustrated in Figures 2 and S6. In addition, it is noted that the intrinsic ΔV_{in}s of J-TMDs can result in the photo-generated electron and hole separation at the J-TMDs layer according to previous studies (Li et al., 2018; Lian et al., 2019; Thanh et al., 2020; Zhang et al., 2020). Thus, the band structures of J-TMDs can be simplified as the oblique band levels. As a consequent, the photo-generated carrier can be transferred at the $CsPbI_3$/J-TMDs contact region induced by the band offsets and J-TMDs layer induced by the intrinsic ΔV_{in}s of J-TMDs. Thus, in order to understand the band offsets and charge transfer at the $CsPbI_3$J-TMDs heterojunctions, the band alignment diagrams of CsI/J-TMDs and PbI/J-TMDs heterojunctions are summarized in Figures 2B and S6B.

Transport properties

To further understand the carrier transfer at the $CsPbI_3$/J-TMDs heterojunctions, energy band diagrams of $CsPbI_3$/J-TMDs heterojunctions are illustrated in Figure 4. The energy levels of isolated $CsPbI_3$ surface and J-TMDs layer are referenced to the vacuum level. The calculated work function (WF) of isolated CsI surface, PbI surface, and monolayer MoS_2 are 4.65, 5.23, and 5.22 eV, respectively, which are consistent with previous studies (Cao et al., 2020; Matter, 2020). The carriers will flow until Fermi levels are lined up when perovskite surface and MoS_2 contact. It is thought that there is a negative vacuum barrier (ΔV) between CsI surface and MoS_2 layer upon forming CsI/MoS_2 heterojunction with equilibrium Fermi level. As a result, CsI surface and MoS_2 layer in CsI/MoS_2 heterojunction demonstrate the upward and downward bending band levels, respectively (see Figure 4A), which will induce a positive energy barrier (ΔT) at when carrier transfers from CsI surface to MoS_2 layer. Such vacuum barrier ΔV can be regarded as the driving force for carrier transfer at the heterojunction; such energy barrier ΔT hampers the carrier transfer efficiency at

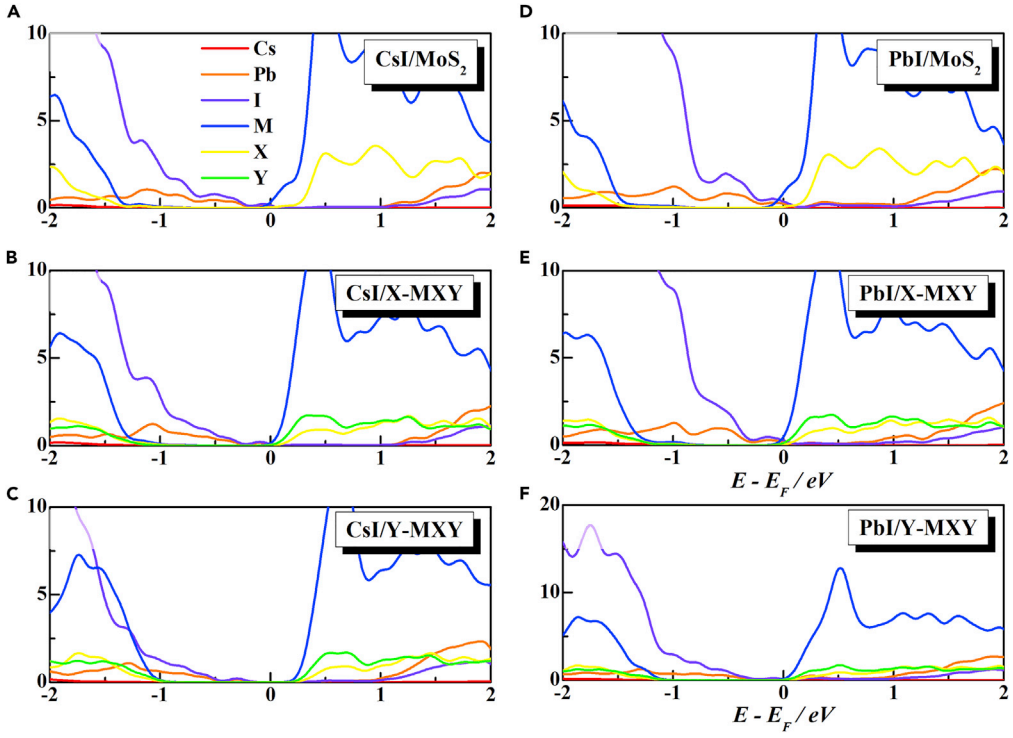

Figure 3. Projected density of states for $CsPbI_3$/J-TMDs heterojunctions

(A–C) Projected density of states for the heterojunctions based on CsI configuration.

(D–F) Projected density of states for the heterojunctions based on PbI configuration.

the heterojunctions. Compared to the CsI/MoS_2 heterojunction, similar ΔV and ΔT are observed for the CsI/MoSSe heterojunction, except for the lower absolute values, because the MoSSe monolayer possesses the lower WF than the MoS_2 monolayer. Moreover, the CsI/Se-MoSSe heterojunction shows the lower ΔV and ΔT than the CsI/S-MoSSe heterojunction, because the WF of MoSSe monolayer at the SE atomic layer is lower than that at the S atomic layer. This inconsistent WF induces the intrinsic potential difference ΔV_{in} for MoSSe monolayer whose direction points from SE atomic layer to S atomic layer, which promotes electron transfer from the SE atomic layer to the S atomic layer of MoSSe monolayer. It means that CsI/MoSSe heterojunction, especially the CsI/Se-MoSSe heterojunction whose ΔV_{in} direction points from SE atomic layer to S atomic layer, shows the weaker carrier transfer drive force and higher carrier transfer efficiency compared to the CsI/MoS_2 heterojunction. According to the above analysis, increasing the intrinsic ΔV_{in} by altering the X/Y and M atoms of MXY can further decrease the WF of J-TMD monolayer, as listed in Table S4. As a result, the WF of J-TMD, especially at the Y atomic layer, is lower than that of CsI surface. Consequently, the negative ΔV can turn into positive ΔV, and ΔT continues to decrease for CsI/J-TMD heterojunction with large ΔV_{in}, as the ΔV and ΔT for CsI/Te-SMoTe and CsI/Te-SWTe heterojunctions displayed in Figure S8A. That is why the CsI/Te-SMoTe and CsI/Te-SWTe heterojunctions show the inversely type-II band alignments. It also indicates that the carrier transfer efficiency for CsI/J-TMD heterojunction can be improved by increasing the ΔV_{in} of J-TMD.

Different from the CsI/MoS_2 heterojunctions, PbI/MoS_2 heterojunctions demonstrate a positive ΔV because the WF of PbI surface is larger than that of MoS_2 monolayer (see Figure 4D and Table S4). This positive ΔV hampers the electron transfers from the perovskite surface to MoS_2 layer. Meanwhile, PbI surface and MoS_2 layer in PbI/MoS_2 heterojunction demonstrate the downward and upward bending band levels, respectively (see Figure 4D), which will induce a much lower energy barrier ΔT when the carrier transfers from PbI surface to the MoS_2 layer. Different from the MoS_2 monolayer, the MoSSe monolayer with an intrinsic ΔV_{in} exhibits the lower WF than PbI surface, which resulting in the larger ΔV for PbI/MoSSe heterojunction than PbI/MoS_2 heterojunction. It suggests the weaker drive force for charge transfer from perovskite to the MoSSe layer. Theoretically, the larger ΔV will induce the stronger band

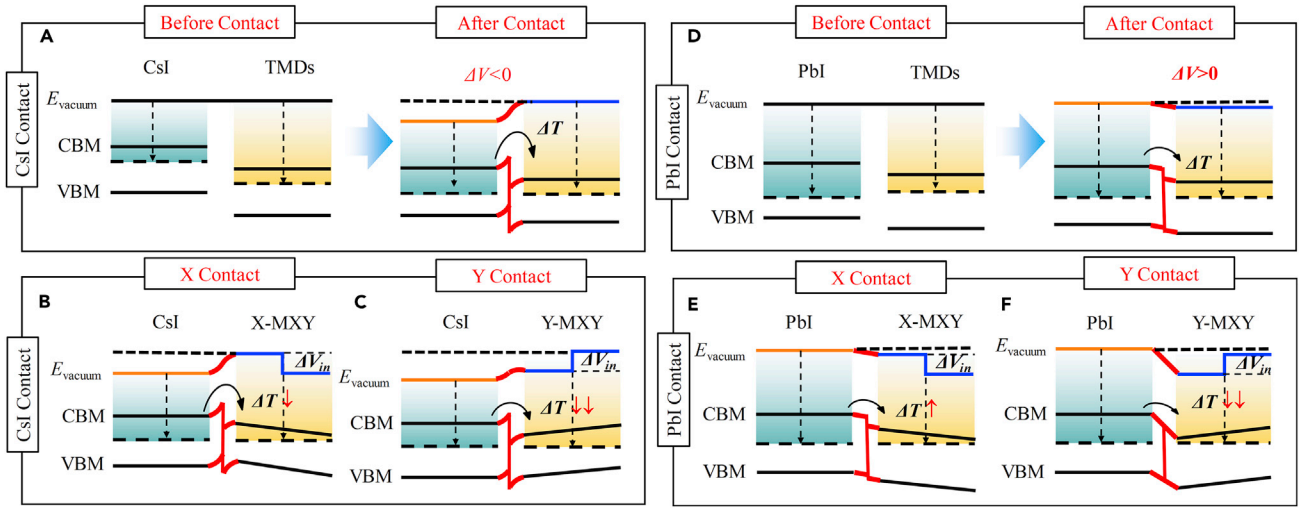

Figure 4. Schematic energy band diagrams for $CsPbI_3$/J-TMDs heterojunctions

(A–C) Schematic energy band diagrams for the heterojunctions based on CsI configuration.

(D–F) Schematic energy band diagrams for the heterojunctions based on PbI configuration.

bending, which leads to the smaller ΔT for PbI/MoSSe heterojunction, in particular the PbI/Se-MoSSe heterojunction. As the intrinsic ΔV_{in} increases, the WFs of J-TMDs will continue to decrease, which theoretically leads to the increasing ΔV and reducing ΔT for PbI/J-TMDs heterojunction, especially with the PbI/Y-MXY configuration, as displayed in Figures 4E and 4F. It is noted that PbI surface is p-type semiconductor, suggesting that hole transfers from PbI surface to J-TMDs layer. It will raise the band levels of J-TMDs layer. Meanwhile, the intrinsic ΔV_{in} of J-TMD promotes hole transfers from the Y atomic layer to the X atomic layer of J-TMDs, which further increases the band levels of X atomic layer of J-TMDs. Consequently, the ΔT of PbI/J-TMD heterojunction with PbI/X-MXY configuration may be enlarged as the intrinsic ΔV_{in} increases.

As an evidence of the analysis above, the planar-averaged electrostatics potentials (top) and planar-averaged charge density differences (bottom) of the $CsPbI_3$/J-TMDs heterojunctions are demonstrated in Figure 5 and detailed in Figures S9–S11. It can be found that electrons and holes are mainly accumulated at the MoS_2 and CsI layers of CsI/MoS_2 heterojunction, respectively, suggesting that electrons transfer from the CsI surface to the MoS_2 layer of heterojunction. Moreover, the charge transfer decreases when the MoS_2 layer of heterojunction is replaced by J-TMDs layer with intrinsic ΔV_{in} to form CsI/J-TMDs heterojunction, in particular the heterojunction with CsI/Y-MXY configurations, as displayed in Figures 5A–5C. The charge transfer of CsI/J-TMDs heterojunction further decreases with the enlarging intrinsic ΔV_{in} (see Figure S12. These characters further confirm the above variation of ΔV for CsI/J-TMDs heterojunctions. Different from CsI/J-TMDs heterojunction, some electrons are accumulated at the PbI surface of PbI/J-TMDs heterojunctions, especially the heterojunction with PbI/X-MXY configuration, because holes are transferred from p-type PbI surface to J-TMDs. This is consistent with the above analysis of the band diagram. Moreover, the hole (electron) transfer are enhanced (reduced) for PbI/J-TMDs heterojunctions as the intrinsic ΔV_{in} enlarges, which is in good agreement with the above ΔV for PbI/J-TMDs heterojunctions.

It is noted that the above analyzed ΔT can be quantitatively marked in the electrostatics potentials of heterojunction, as seen in the yellow square in Figure 5. The detailed ΔTs of CsI/J-TMDs and PbI/J-TMDs heterojunctions are illustrated in Figures 5D and 5H. It can be found that the ΔTs of CsI/J-TMDs heterojunctions decline with the enlarging intrinsic ΔV_{in}. Moreover, the ΔT reduction of CsI/J-TMDs heterojunctions with CsI/Y-MXY configuration is more significant than that with CsI/X-MXY configuration. It is thought that the carrier transfer efficiency at the CsI/J-TMDs heterojunctions, especially the heterojunction with CsI/Y-MXY configuration, increases with the enlarging intrinsic ΔV_{in}. In contrast, the ΔTs of PbI/J-TMDs heterojunctions with PbI/X-MXY configuration enhance, whereas those of PbI/J-TMDs heterojunctions with PbI/Y-MXY configuration decline with the enlarging intrinsic

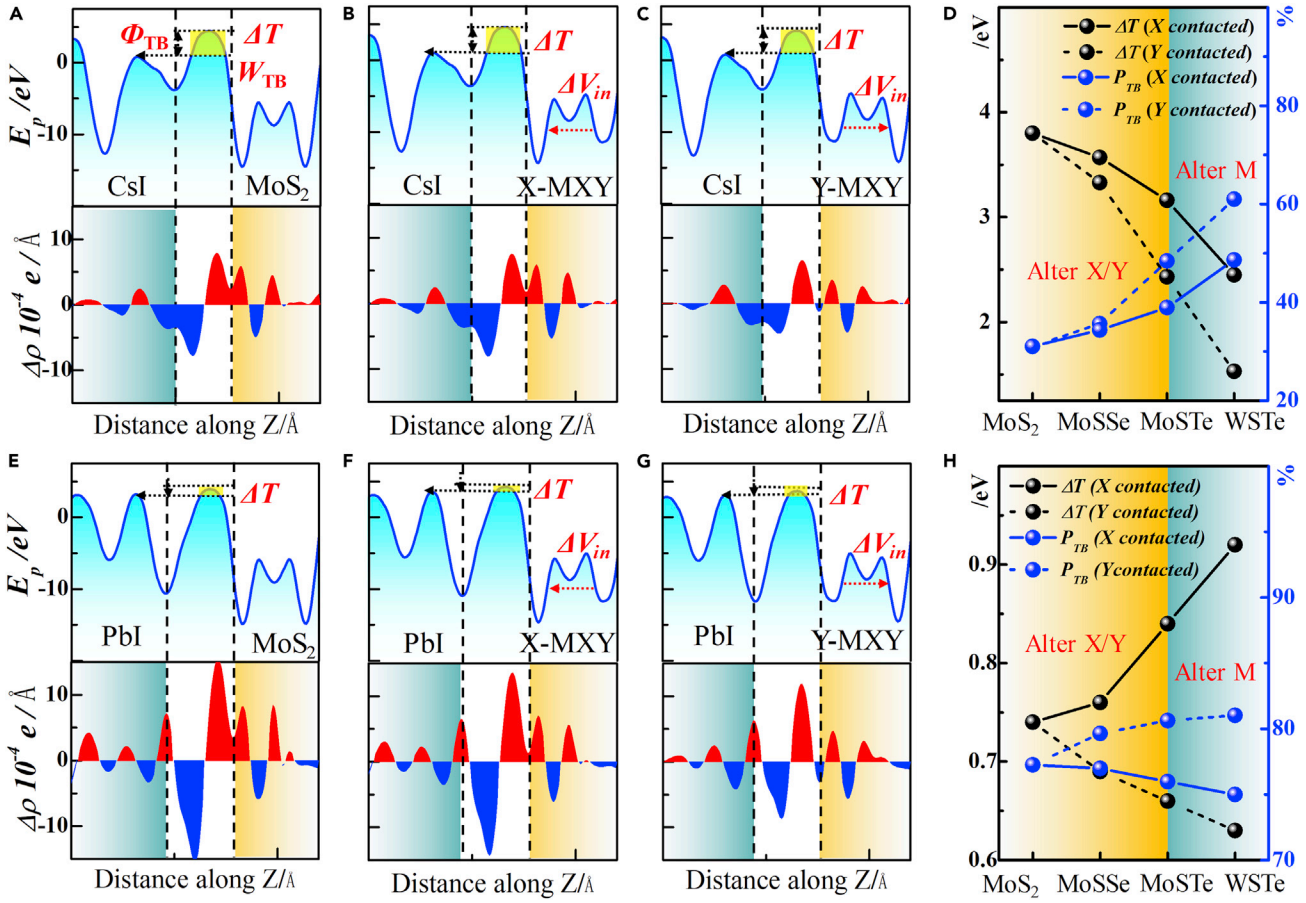

Figure 5. Interfacial transportation properties for $CsPbI_3$/J-TMDs heterojunctions

(A–C) Planar-averaged electrostatic potentials and charge density differences for the heterojunctions based on CsI configuration.

(D) The tunnel barriers and tunneling probabilities of CsI/J-TMDs as a function of intrinsic ΔV_{in}.

(E–G) Planar-averaged electrostatic potentials and charge density differences for the heterojunctions based on PbI configuration.

(H) The tunnel barriers and tunneling probabilities of PbI/J-TMDs as a function of intrinsic ΔV_{in}

ΔV_{in}, which are consistent with the above analysis of ΔT for PbI/J-TMDs heterojunctions from band diagram.

To directly show the carrier transfer efficiency at the $CsPbI_3$/J-TMDs heterojunctions, the tunneling probability (P_{TB}) is calculated as follows (Yuan et al., 2020, 2021)

$$P_{TB} = \exp\left(-2w_{TB} \times \frac{\sqrt{2m_e\Phi_{TB}}}{\hbar}\right) \quad \text{(Equation 1)}$$

where m_e is the free electron mass of isolated $CsPbI_3$ of about 0.18 m_0, $\hbar$ is the reduced Plank's constant, and Φ_{TB} and W_{TB} are the height and full width at half maximum of the tunneling barrier, respectively. The tunneling probability P_{TB} of $CsPbI_3$/J-TMDs heterojunctions are detailed at Figures 5D and 5H. For the CsI/MoS_2 heterojunction, the ΔT is about 3.8 eV with corresponding P_{TB} of about 31.06%, which is consistent with previous studies, (He et al., 2019) indicating a poor carrier transfer efficiency at the CsI/MoS_2 heterojunction. Moreover, as illustrated in Figure 5D, when intrinsic ΔV_{in} is introduced into J-TMDs to form CsI/J-TMDs heterojunctions, the ΔT decreases and P_{TB} increases with the enlarging intrinsic ΔV_{in}, irrespective of the ΔV_{in} direction, indicating an improved carrier transfer efficiency. In addition, the ΔT reaches to the lowest 1.53 eV with a highest P_{TB} of about 60.98% in CsI/Te-WSTe heterojunction. Better than CsI/MoS_2 heterojunction, the ΔT reduces to 0.74 eV with P_{TB} of about 77.26% in the PbI/MoS_2 heterojunction which is about twice as much as CsI/MoS_2 heterojunction. Consistent with above analysis of ΔT and ΔV_{in} in Figure 4, the ΔT (P_{TB}) of PbI/J-TMD heterojunction enlarges (reduces) in PbI/X-MXY configuration, while being

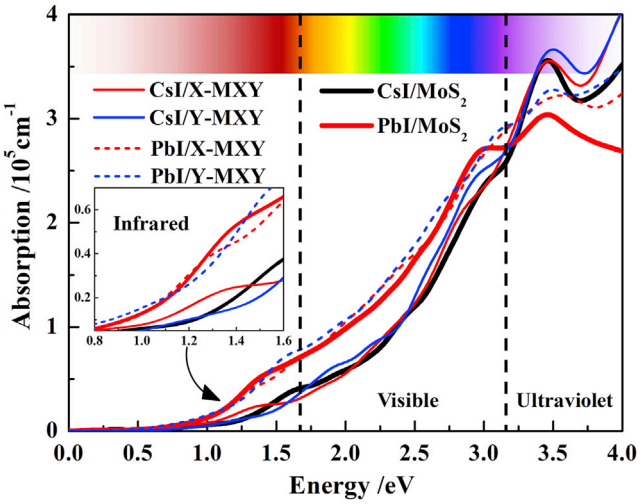

Figure 6. Calculated absorption coefficients for $CsPbI_3$/J-TMDs heterojunctions

reduced (enlarges) in PbI/Y-MXY configuration as the intrinsic ΔV_{in} increases. In addition, the P_{TB} of PbI/Te-WSTe heterojunction reaches a maximum of 81.02% and a minimum ΔT of 0.63 eV. Those dates with an enhanced P_{TB} suggests an improved carrier transfer efficiency in $CsPbI_3$/J-TMDs heterojunctions compared with $CsPbI_3/MoS_2$ heterojunctions, indicating an effectively way to improve the interfacial transportation by introduce ΔV_{in} to construct $CsPbI_3$/J-TMDs heterojunctions.

Optical properties

It is important to study the light absorption capacity of heterojunction for its application in optoelectronic devices. The absorption spectra is calculated by the following formula

$$\alpha(\omega) = \left(\sqrt{2}\right)\omega\omega\left)\left(\omega\right)(\omega)^2\right]^{\frac{1}{2}} \quad \text{(Equation 2)}$$

where α is the absorption coefficient, ω is optical frequency, and $\varepsilon_1(\omega)^2$ and $\varepsilon_2(\omega)^2$ are the real and imaginary parts of the dielectric function, respectively. Figure 6 demonstrated the calculated absorption coefficients of the $CsPbI_3$/J-TMDs heterojunctions, and it seems a higher optical absorption of those heterojunctions with PbI configuration rather than CsI configuration at infrared-visible range, but a lower absorption in UV region, result from the former stronger carrier transfer efficiency analyzed above. Moreover, the optical absorption of those CsI/J-TMDs heterojunctions drops in infrared region with increase in visible-ultraviolet range, and that trend enlarges further as the intrinsic ΔV_{in} increases, irrespective of the configuration and the direction of ΔV_{in}, as detailed in Figure S13. In UV region, those CsI/J-TMDs heterojunctions with CsI/Y-MXY configuration have higher absorption than those CsI/J-TMDs heterojunctions with CsI/X-MXY configuration, which is in good agreement with the above carrier transfer efficiency analyses. Same characteristics are observed in PbI/J-TMDs heterojunctions. These results suggest that forming $CsPbI_3$/J-TMDs heterojunction with ΔV_{in} has a significant enhancement for its application in photoelectric devices.

In summary, the optoelectronic properties of $CsPbI_3$/J-TMDs heterojunctions have been modulated by the intrinsic ΔV_{in} here. It is found the heterojunction with a larger ΔV_{in} pointing away from the interface possesses a smaller band offset with higher carrier transfer efficiency and optical absorption, but a reversed type-II band alignment occurs when ΔV_{in} increases further, suggesting that carrier transport paths can be reversed by modulating the contact configuration of the J-TMDs in the heterojunctions. As a result, the $CsPbI_3$/MoSSe heterojunction is suggested in this work with P_{TB} of about 79.65%.

Conclusions

Here, the optoelectronic properties of $CsPbI_3$/J-TMDs heterojunctions are studied by using the first-principle calculation to reveal the influence of intrinsic ΔV_{in} on the interfacial transport properties of

optoelectronic devices. Remarkably, we found that a modulable ΔV_{in} exists in J-TMDs, which could be modulated significantly by altering chalcogens or modulated slightly by altering metals of J-TMDs. Moreover, the $CsPbI_3$/J-TMDs heterojunctions have a type-II band alignment with the VBM and CBM located at the perovskite and J-TMDs parts, respectively, indicating an ability for separating electrons and holes continuously and effectively, similar to $CsPbI_3/MoS_2$ heterojunctions. In addition, the type-II band alignment is reversed when ΔV_{in} deviates from the interface and increases further, suggesting that carrier transport paths can be reversed by modulating the contact configuration of J-TMDs in the heterojunctions. Meanwhile, a better optoelectronic performance is found in the heterojunction based on PbI configuration rather than CsI configuration, resulting from the former higher work function and more complete structural framework. The band offset, carrier transfer efficiency and optical absorption are directly determined by the intensity and direction of ΔV_{in}. In addition, the heterojunction with a larger ΔV_{in} pointing away from the interface possess a smaller band offset with higher carrier transfer efficiency and optical absorption, and $CsPbI_3$/MoSSe heterojunction with P_{TB} of about 79.65% is suggested in this work. Overall, modulating the intensity and direction of ΔV_{in} can facilitate to formation type-II $CsPbI_3$/J-TMDs heterojunctions with excellent interfacial carrier transfer efficiency, our findings are vital to design and realize novel high-performance lead halide perovskite-based optoelectronic device.

Limitations of the study

In this work, we introduced the interfacial transport modulation of lead halide perovskite by the intrinsic potential difference of asymmetrical 2D materials Janus TMDs based on $CsPbI_3$/J-TMDs heterojunctions. The heterojunctions with ΔV_{in} show excellent interfacial charge transport and absorption propriety. It would be more interesting to study the optoelectronic device based on $CsPbI_3$/J-TMDs heterojunctions with ΔV_{in} in experiment.

STAR★METHODS

Detailed methods are provided in the online version of this paper and include the following:

- KEY RESOURCES TABLE
- RESOURCE AVAILABILITY
  - Lead contact
  - Materials availability
  - Data and code availability
- EXPERIMENTAL MODEL AND SUBJECT DETAILS
- METHOD DETAILS
- QUANTIFICATION AND STATISTICAL ANALYSIS
- ADDITIONAL RESOURCES

SUPPLEMENTAL INFORMATION

Supplemental information can be found online at https://doi.org/10.1016/j.isci.2022.103872.

ACKNOWLEDGMENTS

This work was financially supported by the National Key Research and Development Program of China (2021YFA0715600, 2018YFB2202900), National Natural Science Foundation of China (52192610, 61804111), the 111 Project (B12026), Initiative Postdocs Supporting Program (BX20180234), China Postdoctoral Science Foundation (2018M643578), Fundamental Research Funds for the Central Universities, and the Innovation Fund of Xidian University. The numerical calculations in this paper have been done on the HPC system of Xidian University.

AUTHOR CONTRIBUTIONS

H.D.Y. carried out DFT calculations, data analysis, and wrote the manuscript. J.J.C. and J. S. conceived the idea and revised the manuscript. S.Y.Z., J.Y.D., Z.H.L., J.C.Z., and J.Z. contributed to some analysis of the data. J.J.C., J.C.Z., and Y.H. supervised the project.

DECLARATION OF INTERESTS

The authors declare no conflicts of interest.

Received: October 10, 2021
Revised: December 28, 2021
Accepted: January 31, 2022
Published: March 18, 2022

REFERENCES

Allouche, A. (2012). Software news and updates gabedit — a graphical user interface for computational chemistry softwares. J. Comput. Chem. *32*, 174–182. https://doi.org/10.1002/jcc.

Bloechl, P.E. (1994). Projector augmented-wave method. Phys. Rev. B *50*, 17953.

Cao, Y.H., Bai, J.T., and Feng, H.J. (2020). Perovskite termination-dependent charge transport behaviors of the $CsPbI_3$/black phosphorus van der Waals heterostructure. Chin. Phys. Lett. *37*, 107301. https://doi.org/10.1088/0256-307X/37/10/107301.

Dong, L., Lou, J., and Shenoy, V.B. (2017). Large in-plane and vertical piezoelectricity in janus transition metal dichalchogenides. ACS Nano *11*, 8242–8248. https://doi.org/10.1021/acsnano.7b03313.

Er, D., Ye, H., Frey, N.C., Kumar, H., Lou, J., and Shenoy, V.B. (2018). Prediction of enhanced catalytic activity for hydrogen evolution reaction in janus transition metal dichalcogenides. Nano Lett. *18*, 3943–3949. https://doi.org/10.1021/acs.nanolett.8b01335.

Gu, E., Tang, X., Langner, S., Duchstein, P., Zhao, Y., Levchuk, I., Kalancha, V., Stubhan, T., Hauch, J., Egelhaaf, H.J., et al. (2020). Robot-based high-throughput screening of antisolvents for lead halide perovskites. Joule *4*, 1806–1822. https://doi.org/10.1016/j.joule.2020.06.013.

Guo, Y.J., Su, J., Wang, L., Lin, Z., Hao, Y., and Chang, J. (2021). Improved doping and optoelectronic properties of Zn-doped $Cspbbr_3$ perovskite through Mn codoping approach. J. Phys. Chem. Lett. *12*, 3393–3400. https://doi.org/10.1021/acs.jpclett.1c00611.

Guzelturk, B., Winkler, T., Van de Goor, T.W.J., Smith, M.D., Bourelle, S.A., Feldmann, S., Trigo, M., Teitelbaum, S.W., Steinrück, H.G., de la Pena, G.A., et al. (2021). Visualization of dynamic polaronic strain fields in hybrid lead halide perovskites. Nat. Mater. *20*, 618–623. https://doi.org/10.1038/s41563-020-00865-5.

He, J., Su, J., Lin, Z., Zhang, S., Qin, Y., Zhang, J., Chang, J., and Hao, Y. (2019). Theoretical studies of electronic and optical behaviors of all-inorganic $CsPbI_3$ and two-dimensional MS_2 (M = Mo, W) heterostructures. J. Phys. Chem. C *123*, 7158–7165. https://doi.org/10.1021/acs.jpcc.8b12350.

Heyd, J., Peralta, J.E., Scuseria, G.E., and Martin, R.L. (2005). Energy band gaps and lattice parameters evaluated with the Heyd-Scuseria-Ernzerhof screened hybrid functional. J. Chem. Phys. *123*, 174101. https://doi.org/10.1063/1.2085170.

Heyd, J., and Scuseria, G.E. (2004). Efficient hybrid density functional calculations in solids: assessment of the Heyd-Scuseria-Ernzerhof screened coulomb hybrid functional. J. Chem. Phys. *121*, 1187–1192. https://doi.org/10.1063/1.1760074.

Ilawe, N.V., Zimmerman, J.A., and Wong, B.M. (2015). Breaking badly: DFT-D2 gives sizeable errors for tensile strengths in palladium-hydride solids. J. Chem. Theor. Comput. *11*, 5426–5435. https://doi.org/10.1021/acs.jctc.5b00653.

Jiang, Y., Yuan, J., Ni, Y., Yang, J., Wang, Y., Jiu, T., Yuan, M., and Chen, J. (2018). Reduced-dimensional α-$CsPbX_3$ perovskites for efficient and stable photovoltaics. Joule *2*, 1356–1368. https://doi.org/10.1016/j.joule.2018.05.004.

Kadantsev, E.S., and Hawrylak, P. (2012). Electronic structure of a single MoS_2 monolayer. Solid State Commun. *152*, 909–913. https://doi.org/10.1016/j.ssc.2012.02.005.

Lee, Y., Kwon, J., Hwang, E., Ra, C.H., Yoo, W.J., Ahn, J.H., Park, J.H., and Cho, J.H. (2015). High-performance perovskite-graphene hybrid photodetector. Adv. Mater. *27*, 41–46. https://doi.org/10.1002/adma.201402271.

Li, R., Cheng, Y., and Huang, W. (2018). Recent progress of janus 2D transition metal chalcogenides: from theory to experiments. Small *14*, 1–11. https://doi.org/10.1002/smll.201802091.

Li, Y., Zhou, W., Li, Y., Huang, W., Zhang, Z., Chen, G., Wang, H., Wu, G.H., Rolston, N., Vila, R., et al. (2019). Unravelling degradation mechanisms and atomic structure of organic-inorganic halide perovskites by cryo-EM. Joule *3*, 2854–2866. https://doi.org/10.1016/j.joule.2019.08.016.

Lian, J.C., Huang, W.Q., Hu, W., and Huang, G.F. (2019). Electrostatic potential anomaly in 2D Janus transition metal dichalcogenides. Ann. Phys. *531*, 1–10. https://doi.org/10.1002/andp.201900369.

Liu, A., Almeida, D.B., Bonato, L.G., Nagamine, G., Zagonel, L.F., Nogueira, A.F., Padilha, L.A., and Cundiff, S.T. (2021). Multidimensional coherent spectroscopy reveals triplet state coherences in cesium lead-halide perovskite nanocrystals. Sci. Adv. *7*, 1–7. https://doi.org/10.1126/sciadv.abb3594.

Liu, B., Long, M., Cai, M.Q., and Yang, J. (2018). Interface engineering of $CsPbI_3$-black phosphorus van der Waals heterostructure. Appl. Phys. Lett. *112*, 043901. https://doi.org/10.1063/1.5016868.

Lu, A.Y., Zhu, H., Xiao, J., Chuu, C.P., Han, Y., Chiu, M.H., Cheng, C.C., Yang, C.W., Wei, K.H., Yang, Y., et al. (2017). Janus monolayers of transition metal dichalcogenides. Nat. Nanotechnol. *12*, 744–749. https://doi.org/10.1038/nnano.2017.100.

Matter, C. (2020). Interfacial electronic properties of 2D/3D (PtSe2/CsPbX3) perovskite heterostructure 2. J. Phys. Condens. Matter. *32*, 445004.

Nedelcu, G., Protesescu, L., Yakunin, S., Bodnarchuk, M.I., Grotevent, M.J., and Kovalenko, M.V. (2015). Fast anion-exchange in highly luminescent nanocrystals of cesium lead halide perovskites ($CsPbX_3$, X = Cl, Br, I). Nano Lett. *15*, 5635–5640. https://doi.org/10.1021/acs.nanolett.5b02404.

Park, S., Mutz, N., Schultz, T., Blumstengel, S., Han, A., Aljarb, A., Li, L.J., List-Kratochvil, E.J.W., Amsalem, P., and Koch, N. (2018). Direct determination of monolayer MoS_2 and WSe_2 exciton binding energies on insulating and metallic substrates. 2D Mater. *5*, 025003. https://doi.org/10.1088/2053-1583/aaa4ca.

Pedersen, T.G., Latini, S., Thygesen, K.S., Mera, H., and Nikolić, B.K. (2016). Exciton ionization in multilayer transition-metal dichalcogenides. New J. Phys. *18*, 073043. https://doi.org/10.1088/1367-2630/18/7/073043.

Protesescu, L., Yakunin, S., Bodnarchuk, M.I., Krieg, F., Caputo, R., Hendon, C.H., Yang, R.X., Walsh, A., and Kovalenko, M.V. (2015). Nanocrystals of cesium lead halide perovskites ($CsPbX_3$, X = Cl, Br, and I): novel optoelectronic materials showing bright emission with wide color gamut. Nano Lett. *15*, 3692–3696. https://doi.org/10.1021/nl5048779.

Santos, E.J.G., and Kaxiras, E. (2013). Electrically driven tuning of the dielectric constant in MoS_2 layers. ACS Nano *7*, 10741–10746. https://doi.org/10.1021/nn403738b.

Seth, S., Ahmed, T., De, A., and Samanta, A. (2019). Tackling the defects, stability, and photoluminescence of $CsPbX_3$ perovskite nanocrystals. ACS Energy Lett. *4*, 1610–1618. https://doi.org/10.1021/acsenergylett.9b00849.

Song, X., Liu, X., Yu, D., Huo, C., Ji, J., Li, X., Zhang, S., Zou, Y., Zhu, G., Wang, Y., et al. (2018). Boosting two-dimensional MoS_2/$CsPbBr_3$ photodetectors via enhanced light absorbance and interfacial carrier separation. ACS Appl. Mater. Interfaces *10*, 2801–2809. https://doi.org/10.1021/acsami.7b14745.

Tao, W.-L., Mu, Y., Hu, C.-E., Cheng, Y., and Ji, G.-F. (2019). Electronic structure, optical properties, and phonon transport in Janus monolayer PtSSe via first-principles study. Philos. Mag. *99*, 1025–1040. https://doi.org/10.1080/14786435.2019.1572927.

Tao, W., Zhang, C., Zhou, Q., Zhao, Y., and Zhu, H. (2021). Momentarily trapped exciton polaron in two-dimensional lead halide perovskites. Nat. Commun. *12*, 1–8. https://doi.org/10.1038/s41467-021-21721-3.

Tao, W., Zhou, Q., and Zhu, H. (2020). Dynamic polaronic screening for anomalous exciton spin relaxation in two-dimensional lead halide

perovskites. Sci. Adv. *6*, 2–10. https://doi.org/10.1126/sciadv.abb7132.

Thanh, V. Van, Van, N.D., Truong, D. Van, Saito, R., and Hung, N.T. (2020). First-principles study of mechanical, electronic and optical properties of Janus structure in transition metal dichalcogenides. Appl. Surf. Sci. *526*, 146730. https://doi.org/10.1016/j.apsusc.2020.146730.

Tran, F., Laskowski, R., Blaha, P., and Schwarz, K. (2007). Performance on molecules, surfaces, and solids of the Wu-Cohen GGA exchange-correlation energy functional. Phys. Rev. B Condens. Matter *75*, 1–14. https://doi.org/10.1103/PhysRevB.75.115131.

Wang, K., Xing, G., Song, Q., and Xiao, S. (2021a). Micro- and nanostructured lead halide perovskites: from materials to integrations and devices. Adv. Mater. *33*, 1–19. https://doi.org/10.1002/adma.202000306.

Wang, L., Su, J., Guo, Y., Lin, Z., Hao, Y., and Chang, J. (2021b). 97.3% Pb-reduced $CsPb_{1-x}Ge_xBr_3$ perovskite with enhanced phase stability and photovoltaic performance through surface Cu doping. J. Phys. Chem. Lett. *12*, 1098–1103. https://doi.org/10.1021/acs.jpclett.0c03580.

Wang, Yiliu, Wan, Z., Qian, Q., Liu, Y., Kang, Z., Fan, Z., Wang, P., Wang, Yekan, Li, C., Jia, C., et al. (2020). Probing photoelectrical transport in lead halide perovskites with van der Waals contacts. Nat. Nanotechnol. *15*, 768–775. https://doi.org/10.1038/s41565-020-0729-y.

Yin, W.-J., Tan, H.-J., Ding, P.-J., Wen, B., Li, X.-B., Teobaldi, G., and Liu, L.-M. (2021). Recent advances in low-dimensional Janus materials: theoretical and simulation perspectives. Mater. Adv. *2*, 7543–7558. https://doi.org/10.1039/d1ma00660f.

Yuan, H., Su, J., Guo, R., Tian, K., Lin, Z., Zhang, J., Chang, J., and Hao, Y. (2020). Contact barriers modulation of graphene/β-Ga_2O_3 interface for high-performance Ga_2O_3 devices. Appl. Surf. Sci. *527*, 146740. https://doi.org/10.1016/j.apsusc.2020.146740.

Yuan, H., Su, J., Zhang, P., Lin, Z., Zhang, Jincheng, Zhang, Jie, Chang, J., and Hao, Y. (2021). Tuning the intrinsic electric field of janus-TMDs to realize high-performance β-Ga_2O_3 device based on β-Ga_2O_3/janus-TMD heterostructures. Mater. Today Phys. *21*, 100549. https://doi.org/10.1016/j.mtphys.2021.100549.

Yun, S.J., Han, G.H., Kim, H., Duong, D.L., Shin, B.G., Zhao, J., Vu, Q.A., Lee, J., Lee, S.M., and Lee, Y.H. (2017). Telluriding monolayer MoS_2 and WS_2 via alkali metal scooter. Nat. Commun. *8*, 1–10. https://doi.org/10.1038/s41467-017-02238-0.

Zhang, D., Eaton, S.W., Yu, Y., Dou, L., and Yang, P. (2015). Solution-phase synthesis of cesium lead halide perovskite nanowires. J. Am. Chem. Soc. *137*, 9230–9233. https://doi.org/10.1021/jacs.5b05404.

Zhang, L., Yang, Z., Gong, T., Pan, R., Wang, H., Guo, Z., Zhang, H., and Fu, X. (2020). Recent advances in emerging Janus two-dimensional materials: from fundamental physics to device applications. J. Mater. Chem. A. *8*, 8813–8830. https://doi.org/10.1039/d0ta01999b.

Zhang, S., Su, J., Lin, Z., Tian, K., Guo, X., Zhang, J., Chang, J., and Hao, Y. (2019). Beneficial role of organolead halide perovskite $CH_3NH_3PbI_3/SnO_2$ interface: theoretical and experimental study. Adv. Mater. Inter. *6*, 1–9. https://doi.org/10.1002/admi.201900400.

Zhang, Z., Wang, S., Liu, X., Chen, Y., Su, C., Tang, Z., Li, Y., and Xing, G. (2021). Metal halide perovskite/2D material heterostructures: syntheses and applications. Small Methods *5*, 1–36. https://doi.org/10.1002/smtd.202000937.

Zhou, W., Chen, J., Yang, Z., Liu, J., and Ouyang, F. (2019). Geometry and electronic structure of monolayer, bilayer, and multilayer janus WSSe. Phys. Rev. B *99*, 1–7. https://doi.org/10.1103/PhysRevB.99.075160.

Zhou, Y., and Zhao, Y. (2019). Chemical stability and instability of inorganic halide perovskites. Energy Environ. Sci. *12*, 1495–1511. https://doi.org/10.1039/c8ee03559h.

STAR★METHODS

KEY RESOURCES TABLE

REAGENT or RESOURCE	SOURCE	IDENTIFIER
Software and algorithms		
Vienna Ab-initio Simulation Package	Xidian University	VASP 5.4.1

RESOURCE AVAILABILITY

Lead contact

Further information and requests for resources should be directed to and will be fulfilled by the lead contact, Jingjing Chang (jjingchang@xidian.edu.cn).

Materials availability

This study did not generate new unique reagents.

Data and code availability

Any additional information required to reanalyze the data reported in this work paper is available from the Lead Contact upon request.

EXPERIMENTAL MODEL AND SUBJECT DETAILS

Our study does not use experimental models typical in the life sciences.

METHOD DETAILS

All calculations is performed using density functional theory (DFT), as implemented in the *Vienna ab initio simulation package* (VASP) code(Allouche, 2012). The projector-augmented wave (PAW) method is used to describe the interaction between ion cores and valence electrons(Bloechl, 1994). Perdew-Burk-Ernzerhof (PBE) exchange-correlation functional is employed. Van der Waals (vdW) interaction is applied total energies and forces by means of DFT-D2 method(Ilawe et al., 2015; Tran et al., 2007). The cutoff energy of plane-wave is set to be 400 eV. The convergence criterion is set to be 1×10^{-5} eV for the self-consistent process, and all atoms are allowed to be fully relaxed until the atomic Hellmann-Feynman forces are less than 0.01 eV/$Å^{-1}$, respectively. A vacuum of 15 Å is considered along *z* direction to avoid artificial interlayer interactions. A $9 \times 9 \times 1$ k-sampling generated by the Monkhorst-Pack scheme is used for the Brillouin zone integration. The hybrid functional of Heyd-Scuseria-Ernzerhof (HSE06) with the spin−orbital coupling (SOC), which adopts a mixing parameter of 0.25 and a screening parameter of 0.2 $Å^{-1}$ for the Hartree-Fock exchange, is used to correct the electronic structures(Heyd et al., 2005; Heyd and Scuseria, 2004).

The CsPbI3/J-TMDs heterojunctions are composed of 1×1 supercell of CsPbI3 (001) surface and $2 \times \sqrt{3}$ supercell of J-TMDs (001) surface. The average lattice mismatches of CsPbI3/J-TMDs heterojunctions are less than 2.39%.

To obtain the stable CsPbI3/J-TMDs heterojunctions, the binding energies (Eb) of CsPbI3/J-TMDs heterojunctions are calculated using the formula (He et al., 2019)

$$E_b = \left(E_{heterojunction} - E_{pervoskite} - E_{J-TMDs}\right)/N \quad \text{(Equation 3)}$$

where $E_{heterojunction}$, $E_{pervoskite}$ and E_{J-TMDs} respectively represent the energies of $CsPbI_3$/J-TMDs heterojunctions, isolated $CsPbI_3$ surface and monolayer J-TMDs. *N* represents the atoms number of the corresponding $CsPbI_3$/J-TMDs heterojunctions.

The Wannier-Mott exciton binding energy (E_x) estimated based on the effective mass theory can be calculated as(Guo et al., 2021; Wang et al., 2021b)

$$E_x = 13.56 \cdot \frac{m_r^*}{m_e} \cdot \frac{1}{\epsilon^2} \quad \text{(Equation 4)}$$

where m_r^* is the reduced mass given from the effective masses of electron and hole as follow

$$m_r^* = \frac{m_e^* m_h^*}{m_e^* + m_h^*} \quad \text{(Equation 5)}$$

in which ε is the dielectric constant of surrounding material in the Coulomb interaction, m_e* and m_h* are the effective masses of electron and hole, respectively.

The charge density difference along z direction $\Delta\rho(z)$ was characterized as(Zhang et al., 2019)

$$\Delta\rho(z) = \rho(z)_{total} - \rho(z)_{pervoskite} - \rho(z)_{J-TMDs} \quad \text{(Equation 6)}$$

where $\rho(z)_{total}$, $\rho(z)_{pervoskite}$ and $\rho(z)_{J-TMDs}$ are the charge densities of $CsPbI_3$/J-TMDs heterojunctions, isolated $CsPbI_3$ surface and monolayer J-TMDs, respectively.

QUANTIFICATION AND STATISTICAL ANALYSIS

Our study does not include statistical analysis or quantification.

ADDITIONAL RESOURCES

Our study does not include any additional resources.